

Magnetism of the Bilayer Wigner Crystal

Ilya Esterlis, Dmitry Zverevich, Zekun Zhuang, and Alex Levchenko

Department of Physics, University of Wisconsin-Madison, Madison, Wisconsin 53706, USA

(Dated: August 26, 2024)

The multiple-spin exchange frequencies of the bilayer Wigner crystal are determined by the semi-classical method, which is asymptotically exact in the limit of dilute electron densities. The evolution of the exchange frequencies with interlayer distance – as the crystal undergoes a sequence of structural transitions – leads to both ferromagnetic and multi-sublattice antiferromagnetic phases. Extrapolation of the results to higher density suggests a rich magnetic phase diagram of the bilayer Wigner crystal, including the possibility of spin-nematic and valence-bond solid phases. The bilayer crystal is stable to higher electron densities than the monolayer, leading to enhanced magnetic energy scales. Our estimates of the exchange energies suggest some of the magnetic phases may be accessible in recently discovered bilayer Wigner crystals in a transition-metal dichalcogenide system.

I. INTRODUCTION

Bilayer electronic systems, consisting of two Coulomb-coupled two-dimensional (2D) layers of electrons separated by a distance d , exhibit a variety of novel phenomena not possible in a single monolayer. The example of a bilayer two-dimensional electron gas (2DEG) – realized in semiconductor-based systems such as coupled quantum wells and bilayers of certain atomically-thin 2D materials – is of particular interest owing to its relative simplicity and rich phase diagram. Here we will be interested in the behavior of such a system when the electron density is low and the electron-electron interactions are correspondingly strong. While a monolayer 2DEG freezes into a triangular lattice Wigner crystal (WC) [1, 2] at low electron density, the Coulomb interaction between two dilute layers in a bilayer system leads to a variety of new bilayer WC (BLWC) phases. The resulting crystal structure and magnetic order depend on the ratio of d to the average interparticle spacing a within a layer [3–8].

In the present paper we explore the multiple-spin exchange processes and magnetism that arises in such BLWCs. In the dilute limit, where controlled calculations of the exchange couplings are possible, we find a variety of magnetic phases that can be realized as a function of d/a . The extrapolation of our results to higher density suggests a rich magnetic phase diagram of the bilayer 2DEG, including exotic quantum phases.

The Hamiltonian of the bilayer 2DEG is

$$H = \sum_{\ell,i} \frac{\mathbf{p}_{\ell,i}^2}{2m} + \frac{1}{2} \sum_{i \neq j} \frac{e^2}{\epsilon |\mathbf{r}_i^{(1)} - \mathbf{r}_j^{(1)}|} + \frac{1}{2} \sum_{i \neq j} \frac{e^2}{\epsilon |\mathbf{r}_i^{(2)} - \mathbf{r}_j^{(2)}|} + \sum_{ij} \frac{e^2}{\epsilon \sqrt{|\mathbf{r}_i^{(1)} - \mathbf{r}_j^{(2)}|^2 + d^2}}. \quad (1)$$

Here $\ell = 1, 2$ is the layer index and indices i, j label electrons within a layer, i.e., $\mathbf{r}_i^{(\ell)}$ and $\mathbf{p}_{\ell,i}$ refer to the respective position and momentum of electron i in layer ℓ ; m is the effective electron (or hole) mass; and ϵ is the dielectric constant of the environment. Implicit is the presence of a neutralizing background for each layer. We

will consider the situation in which the electron densities in the layers are equal, $n_1 = n_2 \equiv n$. In this case the ground-state properties of the system depend on two dimensionless parameters: the ratio d/a and the usual electron gas parameter $r_s = a/a_B$, where a is related to the density according to $n\pi a^2 = 1$ and $a_B = \hbar^2 \epsilon / me^2$ is the effective Bohr radius of the host semiconductor. The dilute limit, corresponding to large r_s , is the limit of strong intralayer interactions. The strength of interlayer interactions is determined by d/a .

The properties in the extreme dilute limit, obtained by taking $r_s \rightarrow \infty$ with d/a fixed, are well understood. In this regime the system is purely classical and the ground state crystal structure is determined by minimizing the electrostatic Coulomb energy [3–7]. We briefly summarize the results: at infinite interlayer separation the layers form decoupled triangular lattices. As d/a is decreased, the two triangular lattices lock into a staggered triangular lattice structure. Throughout the paper we will follow the nomenclature of Ref. [7] in labeling the various structural phases, where the staggered triangular crystal was called Phase V. Upon further decreasing d/a there is a first-order transition to a staggered rhombic lattice (Phase IV). The angle θ between the primitive vectors continuously changes with decreasing d/a , until the lattice locks into a staggered square structure (Phase III). The staggered square structure remains stable down to a critical value of d/a , beyond which the aspect ratio r changes continuously and the system forms a staggered rectangular lattice (Phase II). This evolution continues to $d/a = 0$, at which point the system becomes a single triangular lattice with twice the original density [9]. The evolution of BLWC structures is summarized in Fig. 1.

Away from the classical $r_s \rightarrow \infty$ limit, there have been attempts to determine aspects of the zero-temperature phase diagram as a function of d/a and r_s , the primary focusing being the quantum melting transition. This includes a perturbative RPA-like treatment of the interlayer interaction [10], a DFT study [8], and quantum Monte Carlo simulation [11]. The most important conclusion common to all these approaches is the enhanced stability of the bilayer crystal phase relative to the monolayer. While the quantum melting of the monolayer WC

occurs at $r_s \approx 35$ [12–15], the bilayer crystal was predicted to be stable down to $r_s \approx 20$ at intermediate values of d/a [11]. Such an enhanced stability of the BLWC is expected, owing to the Coulomb energy gained in the crystal phase from commensurate locking of the lattices in the two layers. As we will elaborate upon below, the stability of the BLWC to higher density (smaller r_s) has a number of interesting consequences. In particular, the energy scales associated with magnetism of the electron crystal – which is the main focus of this paper – increase with increasing density, and the enhanced stability therefore implies higher temperature scales at which interesting magnetic phenomena could be observed.

Perhaps most intriguingly, the existence and enhanced stability of the BLWC were recently confirmed experimentally in a bilayer transition-metal dichalcogenide system [16]. Optical probes indicated formation of insulating states at precisely those density ratios between layers where one would expect commensurate stacking of triangular crystals. The insulating features persisted to significantly higher densities ($r_s \approx 10$) and temperatures ($T \approx 40$ K) than those observed in the corresponding monolayer system [17]. These developments call for a theoretical analysis of the magnetism that could be realized in such a BLWC.

II. APPROACH

As described above, in the dilute limit $r_s \rightarrow \infty$, the Coulomb energy dominates in the Hamiltonian (1), leading to the formation of various classical BLWCs. In the classical approximation, where the kinetic energy is neglected, the electrons forming the BLWC are effectively distinguishable particles and all possible spin states are degenerate. The degeneracy is lifted by the kinetic energy, which allows for quantum tunneling between classical configurations related by permutation of electrons. This leads to an effective “exchange” Hamiltonian in terms of permutation operators acting on the spin degrees of freedom [18–23]:

$$H_{\text{ex}} = \sum_P (-1)^P J_P \hat{P}. \quad (2)$$

The sum is taken over cyclic permutations P of electrons, with \hat{P} the associated permutation operator, and the exchange coupling J_P is one-half the energy splitting associated to tunneling between two electronic configurations related by permutation P . We adopt the convention that $J_P > 0$, the sign of each term in the sum being fixed by the parity of the permutation $(-1)^P$, which, as shown originally by Thouless [18, 19], is positive for exchanges involving an even number of particles and negative for exchanges involving an odd number of particles. The exchange Hamiltonian (2) can be brought into a generalized Heisenberg form by noting that each cyclic permutation P may be decomposed as a product of transpositions, which are in turn expressed in terms of spin operators

$\hat{P}_{ij} = 2(\mathbf{S}_i \cdot \mathbf{S}_j) + 1/2$. Concrete examples of such spin Hamiltonians will be given later.

We will work in the limit of vanishing interlayer tunneling and therefore only consider processes in which particles are exchanged in a single layer, while particles in the opposite layer adjust their positions without exchanging. We refer to them as the “active” and “passive” layers, respectively. With equal layer densities and vanishing interlayer tunneling the exchange Hamiltonian (2) is the sum of two equivalent decoupled magnetic Hamiltonians, one for each layer.

Utilizing the semiclassical instanton method [24], the exchange couplings J_P are found to be [23, 25]

$$J_P = \frac{e^2}{\epsilon_{AB}} \frac{A_P}{r_s^{5/4}} \sqrt{\frac{S_P}{2\pi}} \exp(-\sqrt{r_s} S_P). \quad (3)$$

Here S_P is the Euclidean action evaluated along the classical imaginary-time trajectory that affects the permutation P . The prefactor A_P is related to the “fluctuation determinant”, obtained by integrating over the Gaussian fluctuations about the classical path. The factor e^2/ϵ_{AB} is the effective Hartree energy unit for the 2DEG and sets the overall energy scale. When there is more than one classical path for a given multiparticle permutation the exchanges associated with different paths should be added. The reliability of the semiclassical approximation for the exchange couplings in the dilute regime has been established by comparison with path-integral Monte Carlo simulations of the monolayer WC [26].

In the $r_s \rightarrow \infty$ limit, the dominant exchange is that with the smallest action. In the case of the monolayer WC, the three-particle exchange J_3 has been shown to have the smallest action [20–23]. Hence, as $r_s \rightarrow \infty$, the monolayer WC is a ferromagnet. The situation is richer when we consider the BLWC, as we elaborate upon below.

III. RESULTS

In this section we present results for the classical imaginary-time paths associated with multi-particle exchanges in the BLWC, together with the corresponding actions S_P and prefactors A_P . With knowledge of the actions we can draw conclusions about the magnetism of the BLWC that are asymptotically exact as $r_s \rightarrow \infty$. Our results for the magnetic phases in this limit as a function of d/a [27] are summarized in Fig. 1. By also calculating the prefactors we obtain estimates of the exchange couplings (3) and extend the magnetic phase diagram to finite r_s .

A. Classical actions and magnetism as $r_s \rightarrow \infty$

In the BLWC, the classical action for a given exchange process P is a function of the interlayer distance,

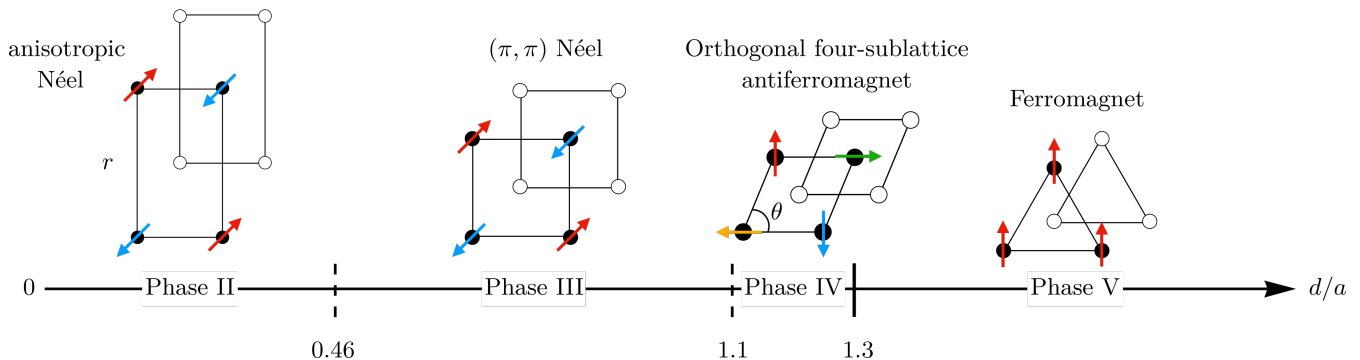


FIG. 1. Magnetic phase diagram of the bilayer WC in the $r_s \rightarrow \infty$ limit as a function of interlayer distance d/a . For clarity, the magnetic order is shown in only one of the two layers. In the staggered triangular crystal (Phase V) the bilayer WC is a ferromagnet. There is a first-order transition when $d/a \approx 1.3$ to Phase IV – a “soft” rhombic phase in which the angle θ between the primitive vectors varies continuously with d/a – possessing orthogonal four-sublattice antiferromagnetic order. A continuous transition occurs at $d/a \approx 1.1$ to the staggered square crystal (Phase III), which has a narrow range of four-sublattice antiferromagnetic order (not shown), transitioning to a (π, π) Néel state when $d/a \approx 1.0$. When $d/a \approx 0.46$ there is a transition to the soft rectangular crystal (Phase II), in which the aspect ratio r varies continuously with d/a , and the system is an anisotropic Néel antiferromagnet, becoming increasingly one-dimensional as $d/a \rightarrow 0$.

$S_P = S_P(d/a)$. We have calculated the classical actions for various exchanges in the BLWC as a function of d/a across the different bilayer geometries described above. This is done by minimizing the Euclidean action

$$S_P = \int_{\mathbf{R}_0}^{P\mathbf{R}_0} dR \sqrt{2m[V(\mathbf{R}) - E_0]}, \quad (4)$$

where $\mathbf{R} = (\mathbf{r}_1^{(1)}, \dots, \mathbf{r}_N^{(1)}, \mathbf{r}_1^{(2)}, \dots, \mathbf{r}_N^{(2)})$ is a $4N$ -dimensional coordinate in the configuration space of the $2N$ electrons (N electrons in each layer), $V(\mathbf{R})$ is the bilayer potential energy given in (1), and \mathbf{R}_0 is the ground state electronic configuration of the BLWC with E_0 the corresponding ground state energy, which has been subtracted for convenience. The integration is done with respect to the arc-length dR in configuration space. In our numerical calculations we discretize the integral (4) into M steps via the trapezoid rule and allow N_{move} electrons in each layer to adjust their positions throughout the exchange, with all other electrons being fixed at their equilibrium BLWC positions. The results presented below are for $M = 16$ and $N_{\text{move}} \approx 100$, the latter depending on the specific lattice geometry and exchange process under consideration. We believe the actions obtained with these parameters to be accurate to within 1%; the convergence with M and N_{move} is discussed in more detail in Appendix A. The electrostatic energy $V(\mathbf{R})$ is efficiently computed via standard Ewald methods [2, 7]. Some additional data concerning the role of the passive layer in the exchange process can be found in Appendix B.

1. Phase V

We start from the staggered triangular phase (Phase V), which is the stable ground state for $1.3 \lesssim d/a < \infty$

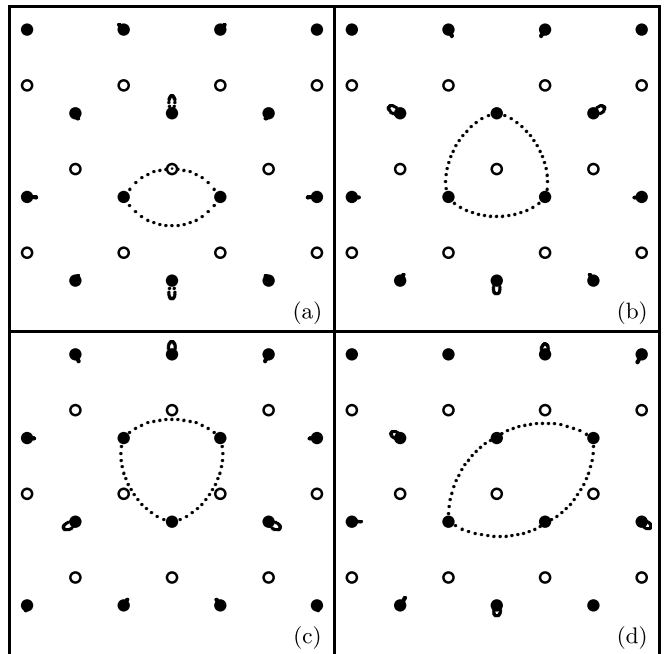


FIG. 2. Paths for (a) 2, (b,c) 3, and (d) 4-particle exchange in the staggered triangular geometry (Phase V) for interlayer separation $d/a \approx 1.5$. Black and white markers correspond to electrons in the active and passive layers, respectively. Dotted lines indicate trajectories of moving particles. We refer to the inequivalent 3-particle exchange paths in Panels (b) and (c) as 3 and 3^* , respectively.

[7]. As a representative example, the 2, 3, and 4-particle exchange paths obtained by minimizing Eq. (4) for $d/a \approx 1.5$ are shown in Fig. 2. For finite d/a there are two inequivalent 3-particle exchange processes, with as-

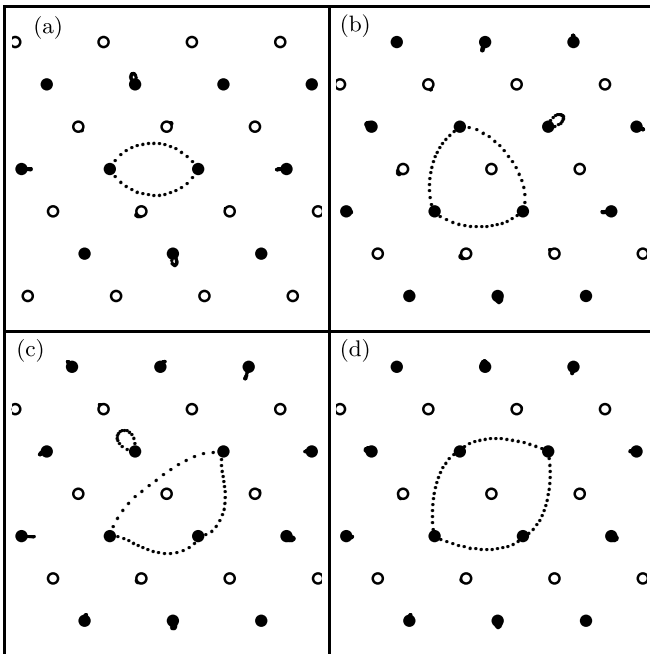


FIG. 3. Paths for (a) 2, (b,c) 3, and (c) 4-particle exchange in the staggered rhombic geometry (Phase IV) for interlayer separation $d/a \approx 1.2$. The 3-particle exchange path in Panel (c), which we refer to as $\tilde{3}$, involves a further neighbor exchange than that in Panel (b), the two paths becoming equivalent in Phase III.

sociated actions S_3 (Fig. 2b) and S_3^* (Fig. 2c), differing in the positions of the neighbors from the opposite layer. Additional data for 5 and 6-particle exchanges are reported in Appendix C.

As $d/a \rightarrow \infty$, we recover the well-known result that the action for 3-particle exchange is the smallest [20, 21, 23]. Upon decreasing d/a , we find S_3^* decreases in magnitude, while all other actions increase; see Fig. 6. (Interestingly, S_3 grows more rapidly than S_2 , the action associated with 2-particle exchange, and there is a crossing point for $d/a \approx 1.5$). The fact that S_3^* has the smallest action throughout Phase V implies that, in the $r_s \rightarrow \infty$ limit, the 3-particle exchange J_3^* is dominant. In the dilute limit, the BLWC in Phase V is therefore a ferromagnet (Fig. 1).

2. Phase IV

When $d/a \approx 1.3$, there is a first-order transition from Phase V to the staggered rhombic phase (Phase IV) [7]. In this phase the angle θ between the primitive vectors of the lattice varies continuously with d/a . Representative 2, 3, and 4-particle exchanges in this phase are shown in Fig. 3 for $d/a \approx 1.2$, corresponding to $\theta \approx 73^\circ$. We have also considered a further neighbor 3-particle exchange path, denoted $\tilde{3}$, involving the long diagonal of the rhombus (Fig. 3c). We include this further neighbor

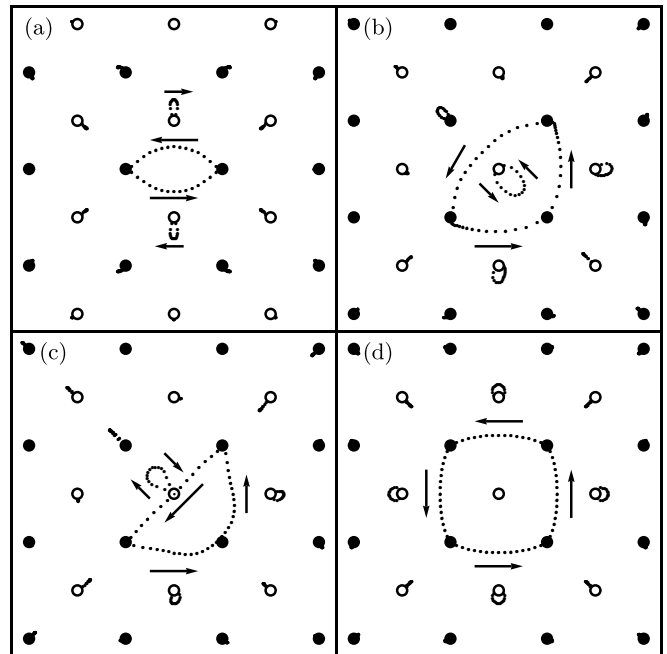


FIG. 4. Paths for (a) 2, (b,c) 3, and (d) 4-particle exchange in the staggered square geometry (Phase III) for interlayer separation $d/a \approx 0.53$. The exchange path in Panel (c) only appears for $d/a \lesssim 0.6$. We refer to this path as $3'$.

path because it becomes equivalent to the more compact 3-particle exchange path involving the short diagonal (Fig. 3b) in Phase III.

Upon entering Phase IV, S_4 , the action associated with 4-particle exchange, abruptly becomes the smallest and remains so throughout this entire structural phase; see Fig. 6. The dominance of the 4-particle exchange in the $r_s \rightarrow \infty$ limit implies that the magnetic ground state of the BLWC in Phase IV in the dilute limit is the orthogonal four-sublattice antiferromagnet [28] (Fig. 1).

3. Phase III

When $d/a \approx 1.1$, the angle θ between primitive vectors locks at 90° and the structure is a staggered square lattice (Phase III) [7]. Representative 2, 3, and 4-particle exchanges in this phase are shown in Fig. 4 for $d/a \approx 0.53$. Over much of this phase we find that there is only a single 3-particle exchange path. However, for $d/a \lesssim 0.4$, another path, which we refer to as $3'$, appears (Fig. 4c).

Within Phase III there is a narrow range $1.0 \lesssim d/a \lesssim 1.1$ over which S_4 remains the smallest action and the magnetic ground state is the 4-sublattice antiferromagnet, as in Phase IV. However, for $d/a \lesssim 1.0$, S_2 becomes smaller than S_4 . The associated 2-particle exchange J_2 therefore dominates as $r_s \rightarrow \infty$ and the magnetic ground state of Phase III in the dilute limit for $d/a \lesssim 1.0$ is the square lattice Néel antiferromagnet (Fig. 1).

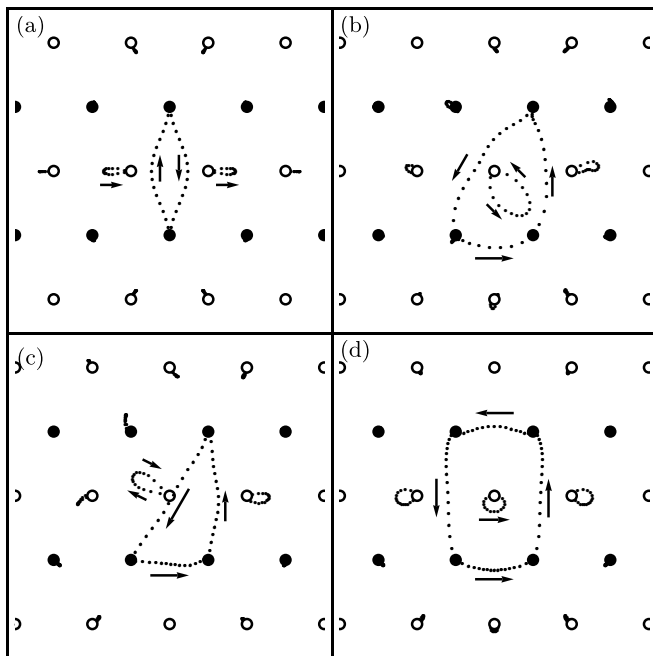


FIG. 5. Exchange paths in staggered rectangular geometry (Phase II) for interlayer separation $d/a \approx 0.27$. Arrows indicate orientation of the paths. (a) 2-particle exchange along the “long” direction of the rectangular lattice. We denote this path 2_{\perp} . The 2-particle exchange path along the “short” direction is the same as that for the monolayer crystal (see Fig. 2a). (b) 3-particle exchange. (c) Additional 3-particle exchange path, referred to as $3'$. (d) 4-particle exchange. Similar paths in the limit $d/a = 0$ have been displayed before in Ref. [25].

4. Phase II

When $d/a \approx 0.46$ there is a phase transition and the aspect ratio r of the square lattice begins to change continuously [7], the lattice becoming increasingly anisotropic with decreasing d/a (Phase II). As $d/a \rightarrow 0$, r goes continuously from $r = 1$ to $r = \sqrt{3} \approx 1.73$, thereby interpolating between the staggered square lattice and a “one-component” triangular lattice at $d/a = 0$. Representative 2, 3, and 4-particle exchanges are shown in Fig. 5 for $d/a \approx 0.27$, corresponding to an aspect ratio $r \approx 1.57$ [29]. We note that similar paths were displayed in Ref. [25] in the limit $d/a = 0$ [30]. There are now two 2-particle exchanges, corresponding to the horizontal and vertical directions. The latter exchange, which we refer to as 2_{\perp} , has a significantly larger action as $d/a \rightarrow 0$ (Fig. 6). As in Phase III, there are two possible 3-particle exchange paths (Fig. 5b,c).

Upon decreasing d/a in Phase II, S_2 decreases monotonically while the actions for all other exchanges increase monotonically; see Fig. 6. The magnetism as $r_s \rightarrow \infty$ is that of an anisotropic Heisenberg antiferromagnet with a corresponding Néel ground state.

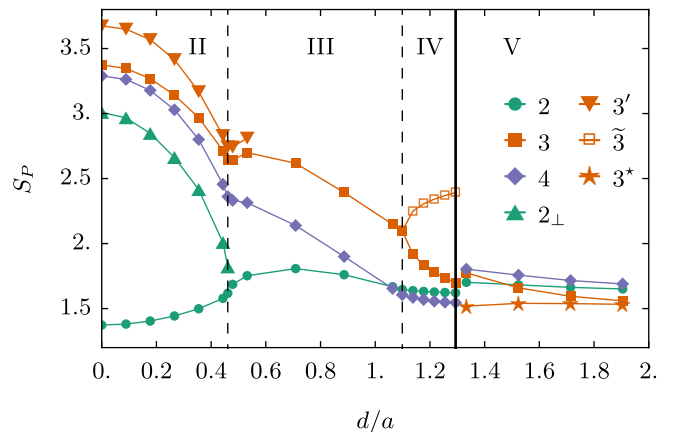


FIG. 6. Dimensionless actions S_P for various 2-, 3-, and 4-particle exchange paths as a function of d/a across the various bilayer WC geometries. Structural phase transitions are indicated by vertical lines; the transition from Phase V \rightarrow Phase IV is discontinuous (solid line), while the transitions Phase IV \rightarrow Phase III and Phase III \rightarrow Phase II are continuous (dashed lines). Labeling of paths is explained in the main text and Figs. 2- 5.

5. Summary: Magnetism of the dilute BLWC

Our results for the magnetic phases of the BLWC in the dilute limit $r_s \rightarrow \infty$ are summarized in Fig. 1. Accompanying the series of structural transitions with varying d/a we find a ferromagnetic phase, as well as two- and four-sublattice antiferromagnetic phases.

For $d/a \lesssim 0.7$, S_2 decreases with decreasing d/a while all other actions are increasing (Fig. 6), S_2 becoming significantly smaller than the actions for other processes as $d/a \rightarrow 0$. In this sense, the BLWC is less magnetically frustrated than the monolayer, where various exchange processes have comparable actions.

B. Prefactors

At finite r_s , the prefactor A_P in Eq. (3) plays a role in determining the dominant exchange cycle. To extend our results away from the $r_s \rightarrow \infty$ limit we have therefore also calculated the prefactors as a function of interlayer distance, $A_P = A_P(d/a)$, across the various crystal structures. In addition to yielding quantitative estimates of the exchanges at finite r_s , the prefactors are of interest in order to understand how the evolution of the phonon spectrum with d/a influences the exchange couplings. Methods to calculate such determinants have been elaborated upon in earlier works [21, 23, 31]. We have followed the approach in Refs. [23, 31], to which we direct the reader for further details. We note that the prefactors converge more slowly with N_{move} than the actions, and it is therefore challenging to rigorously quantify our errors; see Appendix A for more details.

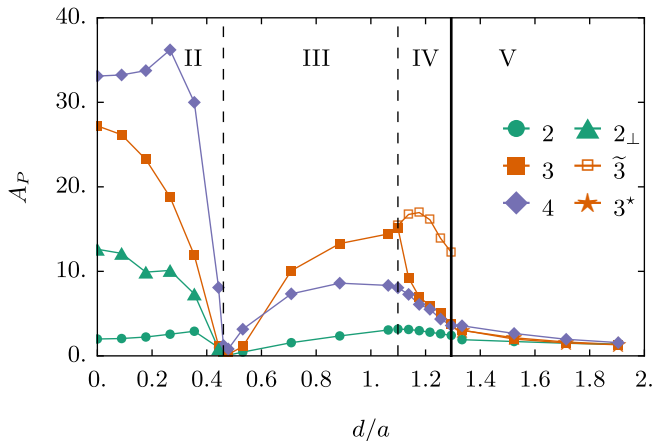


FIG. 7. Dimensionless amplitude prefactors A_P for 2-, 3-, and 4-particle exchanges as a function of d/a across the various bilayer WC geometries. The meaning of paths 2_\perp , $\tilde{3}$, and 3^* is explained in the main text and Figures 4 and 5. The amplitude for path $3'$ in Phases II and III is too large to be put on the present scale; e.g., $A_{3'}(d/a = 0) \approx 60$.

In Fig. 7 we present our results for the prefactors A_P . When d/a is large the prefactors for the different processes considered are all of order one, in agreement with earlier findings on the monolayer WC [21, 23]. As d/a decreases, there is a growing spread in the magnitude of the different prefactors. Some of the A_P become significantly larger than unity at intermediate values of d/a and as $d/a \rightarrow 0$, though these large prefactors are offset by large values of the corresponding actions (see Fig. 6).

A striking feature of the evolution is the rapid decrease of the prefactors at the continuous transition between Phases III and II. It is possible the prefactors exactly vanish at this point, but we cannot say for certain based on the present numerical calculations. We believe this rapid suppression is due to phonon softening at the continuous III \rightarrow II transition and the associated appearance of “flat” directions in the potential landscape. This leads to large fluctuations away from the equilibrium configurations and hence a suppression of the tunneling frequency. However, this cannot be the full story, as a similar suppression of the prefactors is *not* observed at the continuous transition between Phases IV and III. Though we have not pursued the question further here, we believe the behavior of the prefactors near a continuous transition warrants further investigation. We note this evolution has interesting implications, such as the possibility of re-entrant magnetic phases at finite temperature.

C. Exchange couplings and magnetic Hamiltonians

We now combine our results for the classical actions and prefactors according to Eq. (3) to obtain estimates of the various exchanges as a function of r_s and d/a . We also discuss the associated magnetic Hamiltonians in the

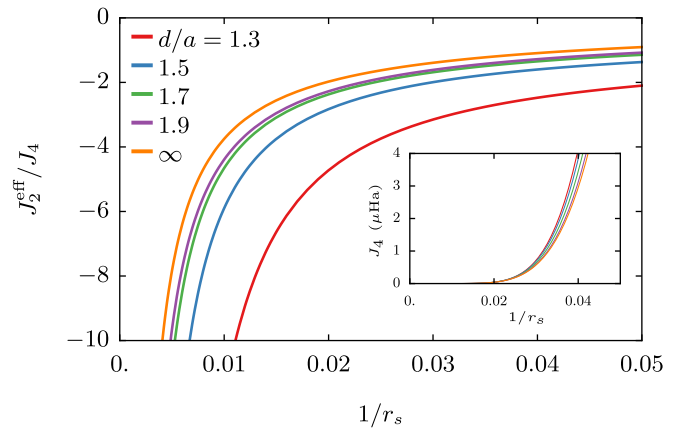


FIG. 8. Ratio of the effective 2-particle exchange $J_2^{\text{eff}} = J_2 - (J_3 + J_3^*)$ to J_4 as a function of $1/r_s$ for different interlayer spacings d/a in Phase V. Inset shows the magnitude of J_4 in micro-Hartree (μHa) as a function of $1/r_s$.

different phases and speculate on the possible magnetic ground states at finite r_s .

1. Phase V

Retaining only 2, 3, and 4-particle exchange, the exchange Hamiltonian (2) in Phase V may be expressed

$$H_{\text{ex}}^{(\text{V})} = J_2^{\text{eff}} \sum_{\text{---}} P_2 + J_4 \sum_{\text{---}} (P_4 + P_4^{-1}). \quad (5)$$

Here the effective 2-particle exchange is $J_2^{\text{eff}} = J_2 - (J_3 + J_3^*)$, which is obtained by reducing 3-particle exchange to a 2-particle term using the spin-1/2 identity $P_{123} + P_{321} = P_{12} + P_{23} + P_{31} - 1$. The ratio J_2^{eff}/J_4 and the magnitude of J_4 are presented in Fig. 8. We find $|J_2^{\text{eff}}|/J_4$ increases with decreasing d/a .

As described in Section III A 1, when $r_s \rightarrow \infty$ the dominance of J_3^* leads to ferromagnetic order. Exact-diagonalization (ED) studies [32] on the ring-exchange Hamiltonian (5) (which also included the 5-particle exchange term) have demonstrated that ferromagnetic order is destroyed for relatively small values of $J_4/|J_2^{\text{eff}}|$ and that, for sufficiently large J_4 , the ground state is possibly a spin-liquid, being characterized by a spin gap, short-range spin correlations, and absence of long range-order. Later exact diagonalization work that included 5 and 6-particle exchange [33] found that a spin-nematic – a magnetically ordered state that preserves time-reversal symmetry but break spin rotation symmetry – could also be stabilized for relatively small values of J_5 and J_6 .

Rather than attempting to identify the precise magnetic ground state at finite r_s , which may depend sensitively on the small couplings associated with larger ring exchange processes, here we would like to highlight that the bilayer coupling simplifies the situation relative to the

monolayer WC. In the monolayer case, ring exchanges involving 4 or more particles become of comparable importance to the (effective) 2-particle exchange at relatively large values of r_s , leading to highly frustrated magnetic interactions and the complex magnetic phase diagram described above [26, 32, 33]. In the bilayer system, however, exchanges involving 4 or more particles are suppressed with decreasing d/a (see Fig. 8 and Appendix C), leading to reduced frustration and enhanced stability of the ferromagnetic state to smaller r_s .

2. Phase III+IV

Phases III and IV are connected continuously, and we therefore discuss the effective exchange Hamiltonian in both phases together. (We could also include Phase II in this discussion, but prefer to leave it for next subsection.) Keeping again only the 2, 3, and 4-particle exchanges, the exchange Hamiltonian in Phases III and IV may be written

$$H_{\text{ex}}^{(\text{III/IV})} = J_2^{\text{eff}} \sum_{\text{---}} P_2 + J_4 \sum_{\text{□}} (P_4 + P_4^{-1}) + \dots \quad (6)$$

It is understood that in Phase IV the 4-particle exchange term is a sum over the elementary rhombus, which becomes a square in Phase III. As in the discussion of Phase V, we have decomposed the 3-particle exchange in terms of 2-particle exchanges. This leads to an effective nearest-neighbor 2-particle exchange $J_2^{\text{eff}} = J_2 - 2(J_3 + \tilde{J}_3)$, as well as a contribution to further-neighbor exchange, indicated by the ellipses. Our results for the ratio J_2^{eff}/J_4 are presented in Fig. 9a. The non-trivial evolution of J_2^{eff}/J_4 with d/a and r_s has interesting implications for the possible magnetic phases, as will be described below. In Fig. 9b we show the ratio J_3/J_4 . We find J_3 is suppressed with decreasing d/a , which implies a diminishing importance of the further-neighbor exchange.

An ED study of the Hamiltonian (6) without the further-neighbor 2-particle exchange terms was carried out in Ref. [28]. The following evolution was found: For $J_2^{\text{eff}}/J_4 \ll 1$ the ground state is the 4-sublattice antiferromagnet mentioned in Sec. III A 2 and III A 3. Upon increasing J_2^{eff}/J_4 there is a transition at $J_2^{\text{eff}}/J_4 \approx 0.2$ to a spin-nematic, followed by a transition to a staggered valence-bond solid (VBS) state when $J_2^{\text{eff}}/J_4 \approx 0.5$. Finally, when $J_2^{\text{eff}}/J_4 > 1$ there is a transition to a Néel antiferromagnet (Sec. III A 3), though we are not aware of any estimates of the transition point.

Our estimates of the exchanges, shown in Fig. 9, suggest all the magnetic phases mentioned above may be realized in the BLWC with varying d/a and r_s . More accurate estimates of the exchange couplings utilizing, e.g., path-integral Monte Carlo methods [26], as well as an extension of the ED study in [28] to include further-neighbor exchange – which is more important for larger values of d/a (see Fig. 9b) – would be useful to clarify this picture.

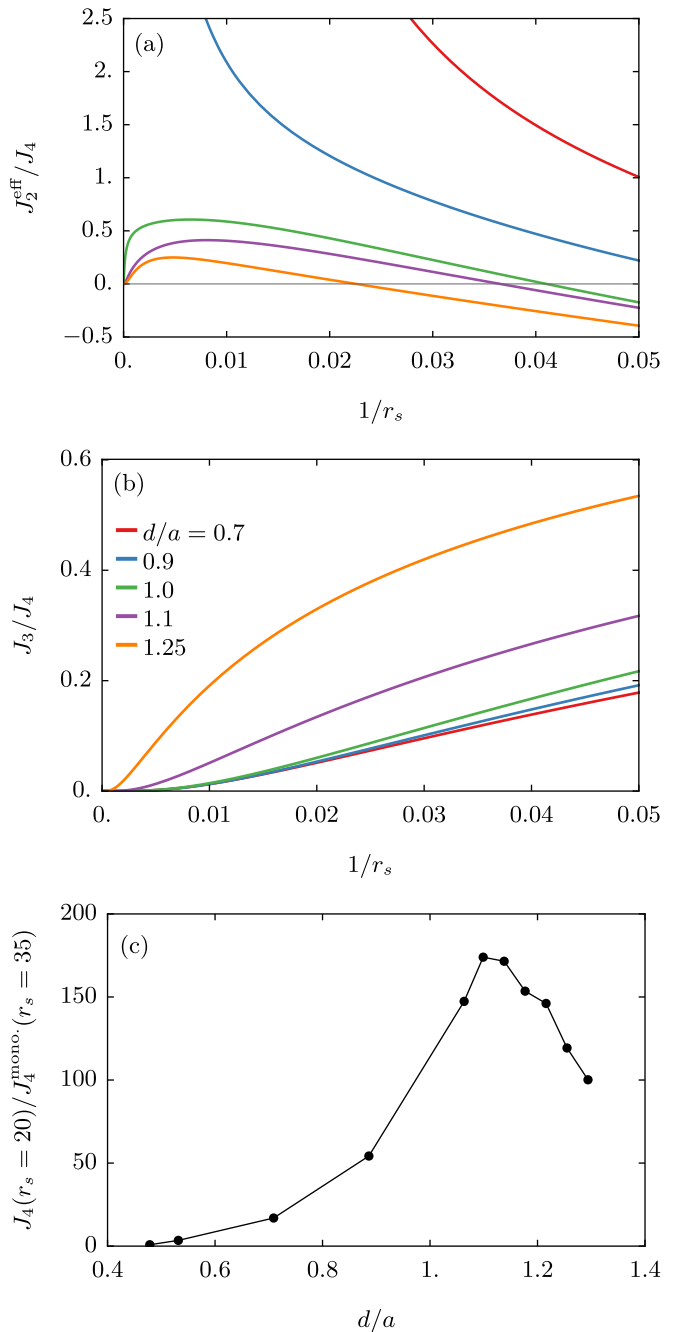


FIG. 9. Exchange couplings in Phases III and IV. (a) Ratio J_2^{eff}/J_4 as a function of $1/r_s$ for $d/a = 0.7, 0.9, 1.0, 1.1, 1.25$, which includes Phase III ($0.46 \lesssim d/a \lesssim 1.1$) and IV ($1.1 \lesssim d/a \lesssim 1.3$). (b) Ratio of 3-particle (which determines the further-neighbor exchange) to the 4-particle exchange. J_3 is significantly suppressed with decreasing d/a . (c) J_4 as a function of d/a at $r_s = 20$, roughly the smallest r_s down to which the bilayer WC is estimated to be stable [11], normalized by the monolayer value J_4^{mono} evaluated at the monolayer melting point $r_s = 35$.

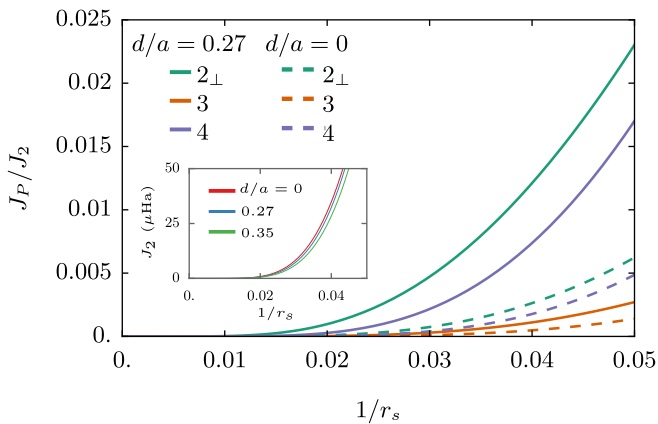


FIG. 10. Exchange couplings in Phase II of the bilayer WC, normalized by J_2 . See Fig. 5 for labeling of exchange paths. Couplings are shown for two values of interlayer distance $d/a = 0.27$ and $d/a = 0$. Inset shows magnitude of J_2 for $d/a = 0, 0.27, 0.35$.

In Fig. 9c we compare the magnitude of J_4 at $r_s = 20$, which is roughly the smallest value of r_s down to which the BLWC is estimated to be stable [11], to the monolayer J_4^{mono} at the monolayer melting point $r_s \approx 35$ [15]. The enhanced stability of the BLWC to higher density suggests the magnetic energy scales may be one to two orders of magnitude larger than in the monolayer.

3. Phase II

In Phase II the dominant exchange is J_2 , the magnetic interactions becoming increasingly anisotropic as $d/a \rightarrow 0$; see Fig. 10. For instance, when $d/a \approx 0.27$ and $r_s = 30$, we find $J_{2\perp}$ (Fig. 5a) is approximately 200 times smaller than J_2 . The magnetism of the BLWC in Phase II will therefore be that of a quasi-1D Heisenberg antiferromagnet over the entire relevant range of r_s . A similar conclusion regarding the magnetism of the BLWC as $d/a \rightarrow 0$ was reached earlier in Ref. [25]. Except in the immediate vicinity of the transition between Phases II and III, the magnitude of J_2 is only weakly dependent on the interlayer distance d/a and is of the order of one micro-Hartree near the melting point at $r_s \approx \sqrt{2} \times 35 \approx 50$ (inset of Fig. 10).

While interlayer tunneling has been neglected throughout this study, as $d/a \rightarrow 0$ it is of interest speculate on the effects of weak tunneling with an associated antiferromagnetic 2-particle exchange J_t between nearest-neighbors in the two layers. The strong anisotropy $J_{2\perp} \ll J_2$ suggests two possible regimes: (i) $J_t \ll J_{2\perp} \ll J_2$ and (ii) $J_{2\perp} \ll J_t \ll J_2$. In Case (i) the problem maps to an anisotropic square lattice Heisenberg model in the limit where next-nearest-neighbor exchange dominates over nearest-neighbor exchange. In this case, we may expect a collinear antiferromagnetic state to be stabilized between the layers via an order-by-disorder mechanism

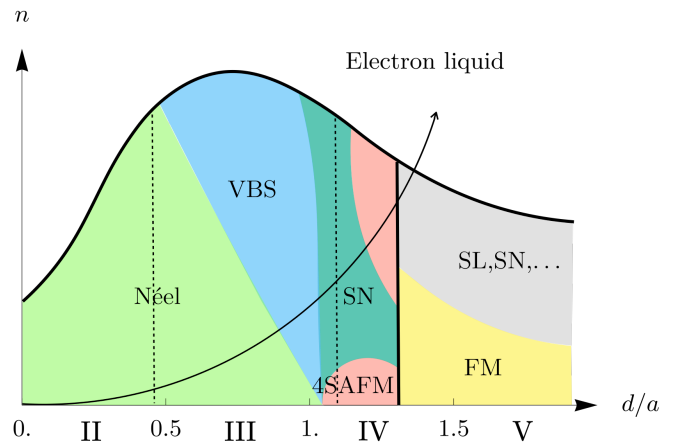


FIG. 11. Schematic zero-temperature phase diagram of the bilayer 2DEG as a function of d/a and density n . Roman numerals indicate the different structural phases. The various magnetic phases are ferromagnet (FM), 4-sublattice antiferromagnet (4SAFM), Néel, spin-nematic (SN), valence-bond solid (VBS), and spin-liquid (SL). At higher density in Phase V we have included some of the candidate magnetic ground states of the multiple-spin exchange model on the triangular lattice, the ellipses indicating that the true ground state depends sensitively on larger ring exchanges not considered here. Arrowed curve indicates a possible experimental path taken by varying n at fixed interlayer separation d . The phase boundaries are sketched, being motivated by earlier work on the liquid-solid transition [11] the present estimates of the exchange couplings in the different geometries. More accurate estimates of the exchanges at finite r_s , as well as the effects of next-nearest-neighbor exchange in Phases II and III, are likely to alter details of the magnetic phase diagram near the melting transition. Effects of finite r_s on the boundaries between structural phases have also not been taken into account.

[34]. In Case (ii) the problem maps to a Heisenberg model on an anisotropic triangular lattice, where the coupling along the chains (J_2) dominates the interchain coupling (J_t). While there have been a variety of numerical and analytical studies of this regime – with proposed ground states including either 1D or 2D spin-liquids, as well as collinear antiferromagnetic order [35] – the nature of the ground state remains, to the best of our knowledge, an open question. Though it is interesting in principle, it seems unlikely current BLWC systems could shed light on the issue given the exceedingly low energy scales associated with both $J_{2\perp}$ and J_t .

IV. DISCUSSION

We have analyzed the multiple spin-exchange processes in the BLWC, from which the magnetic ordering of the crystal is inferred. In the extreme dilute limit $r_s \rightarrow \infty$, we have obtained asymptotically exact results for the magnetic phases of the BLWC as a function of the interlayer distance d/a across the four different structural

phases, finding both ferromagnetic and multi-sublattice antiferromagnetic orders (see Fig. 1). These results have also been extended to finite r_s – where the semiclassical approach is only approximate – and we have argued for a rich set of possible magnetic phases, including a spin-nematic phase, a VBS phase, and possible spin liquids [36]. Estimates of the exchanges suggest significantly enhanced magnetic energy scales at intermediate d/a as compared to the monolayer system.

Our findings are summarized in the schematic phase diagram in Fig. 11. The magnetic phase boundaries are qualitative sketches motivated by our estimates of the exchange couplings. We caution that certain features may be artifacts of the semiclassical approximation and the detailed structure of the phase diagram at finite r_s will require more accurate estimates of the exchanges and analysis of the associated magnetic Hamiltonians. In experimental bilayer systems one typically works with a fixed interlayer distance, sweeping the carrier density in the two layers – such a cut through the phase diagram is shown in Fig. 11.

Given the recent discovery of BLWC phases in a bilayer MoSe₂ system [16], it is of interest to estimate the magnetic energy scales associated to the phases predicted here. In MoSe₂ the effective Hartree energy is roughly 0.7 eV. Depending on the interlayer distance and the density, this yields magnetic energy scales on the order of a few mK up to several hundred mK. The upper end of this range, which is within current experimental reach [37], occurs in the vicinity of Phase III where one may hope to observe a possible VBS or spin-nematic.

There are a number of natural extensions of the present work. For instance, in the case of bilayers with unequal density there are yet more crystal geometries that can be realized [3, 16], likely with further interesting or exotic magnetic phases. The effects of quenched disorder – present in any real 2DEG system – on the magnetic phases we have discussed may also be analyzed with semi-classical methods [23].

Multiple-spin exchange is not the only mechanism for magnetic interactions in the WC. Another interesting possibility is kinetic magnetism [31, 38][39], where magnetic couplings result from the quantum dynamics of defects in the crystal. Such effects are especially important if the WC contains a finite concentration of ground state defects [31], if defects are generated due to quenched disorder [38], or when the BLWC is doped away from commensurate density ratios between layers. The defect hopping amplitudes may be estimated with the same semi-classical methods used here. Interestingly, in the case of the monolayer WC, the energy scales associated with kinetic magnetism are significantly larger than those associated with ring exchange [31, 38].

The ring-exchange magnetism we have described is due to local processes in the BLWC. Because strong local crystalline correlations are built into the *liquid phase* of the 2DEG at large r_s , one may expect that similar processes are relevant [40]. The magnetic characteristics of

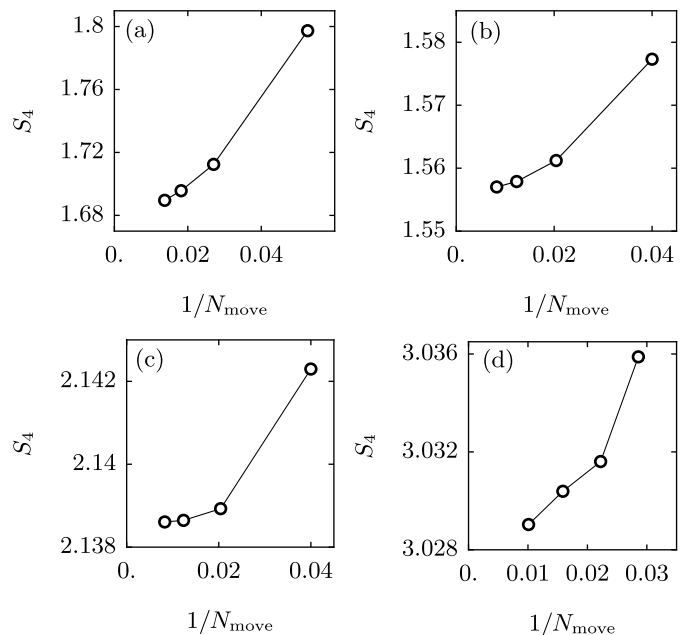


FIG. 12. Convergence of the 4-particle exchange action S_4 with N_{move} for representative values of d/a in each BLWC geometry. (a) $d/a \approx 1.5$ (Phase V), (b) $d/a \approx 1.2$ (Phase IV), (c) $d/a \approx 0.71$ (Phase III), (d) $d/a \approx 0.27$ (Phase II). The action integral is discretized into $M = 16$ slices.

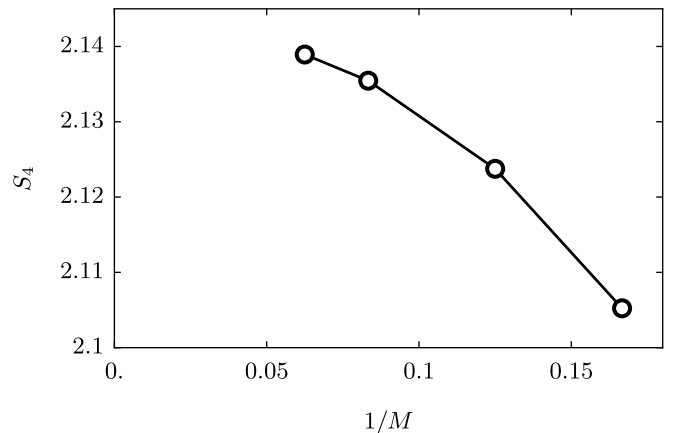


FIG. 13. Convergence of the 4-particle exchange action S_4 with M for $d/a \approx 0.71$ (Phase III). Data is for $N_{\text{move}} = 49$.

the bilayer liquid “inherited” from the proximate crystal may be quite interesting.

ACKNOWLEDGMENTS

The authors are grateful to K. S. Kim for many useful discussions, especially concerning technical aspects of the calculations. One of us (I.E.) acknowledges H. Park, J. Sung, P. Volkov, Y. Yang, S. Zhang, and Y. Zhou for helpful discussions on related work, and would

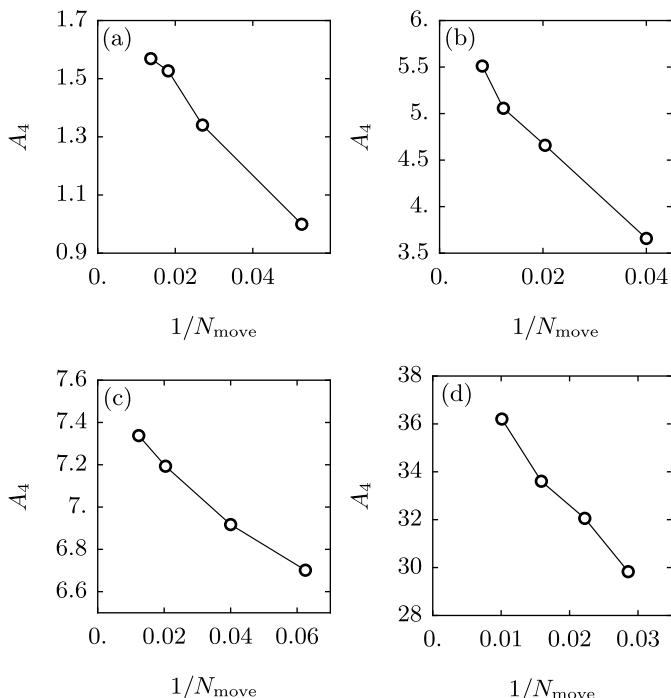


FIG. 14. Convergence of the 4-particle exchange prefactor A_4 with N_{move} for representative values of d/a in each BLWC geometry. (a) $d/a \approx 1.5$ (Phase V), (b) $d/a \approx 1.2$ (Phase IV), (c) $d/a \approx 0.71$ (Phase III), (d) $d/a \approx 0.27$ (Phase II). The action integral is discretized into $M = 16$ slices.

also especially like to thank E. Demler and Y. Wang for many fruitful discussions regarding bilayer Wigner crystals. This research project was financially supported by the National Science Foundation Grant No. DMR-2203411 (D.Z. and Z.Z.) and H. I. Romnes Faculty Fellowship provided by the University of Wisconsin-Madison Office of the Vice Chancellor for Research and Graduate Education with funding from the Wisconsin Alumni Research Foundation (A.L.). I.E. was supported by the University of Wisconsin - Madison. This work was performed in part at Aspen Center for Physics, during the program “Quantum Matter Through the Lens of Moiré Materials”, which is supported by National Science Foundation grant PHY-2210452.

Appendix A: Convergence

To calculate the classical imaginary-time trajectories for a particular ring exchange process we minimize the action (4). This involves two approximations: (1) We allow only a finite number N_{move} of electrons to adjust their positions in each layer and (2) the integral (4) is discretized into M steps.

As an example, in Fig. 12 we present data for convergence of S_4 with increasing N_{move} and $M = 16$, for a representative value of d/a in each of the different BLWC ge-

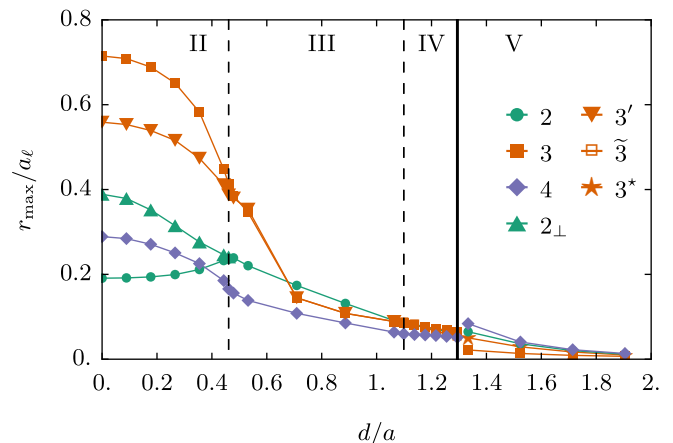


FIG. 15. Maximal displacement r_{max} of a particle away from its equilibrium lattice position in the passive layer as a function of d/a for various exchanges, expressed in units of the lattice constant a_ℓ for the corresponding geometry. Labeling corresponds to that in Figs. 2-5.

ometries. The action is well-converged for $N_{\text{move}} \gtrsim 100$, the difference between the value of S_4 extrapolated to $N \rightarrow \infty$ and that at the largest value of N_{move} being less than 1%. The same is true for other values of d/a and other ring exchange processes.

The convergence of the action with M is shown in Fig. 13, taking S_4 with $d/a \approx 0.71$ (Phase III) and $N_{\text{move}} = 49$ as a representative example. We find the difference between the value of S_4 extrapolated to $M \rightarrow \infty$ and that $M = 16$ is $\lesssim 0.1\%$. Taken together with the convergence with N_{move} , we believe our results for the actions should be accurate to within less than 1%.

In Fig. 14 we show the convergence of the prefactor A_4 at $M = 16$ with increasing N_{move} . The prefactor evidently converges more slowly than the action and, in many cases, the evolution with N_{move} does not admit a well-defined extrapolation to $N_{\text{move}} \rightarrow \infty$. In the main text we therefore report the value of A_P for the largest value of N_{move} used for a particular ring exchange and value of d/a . In those cases where an extrapolation to $N_{\text{move}} \rightarrow \infty$ is possible, we find our errors are $\lesssim 10\%$.

Appendix B: Role of the passive layer

When the interlayer coupling is weak ($d/a \gg 1$), electrons in the passive layer do not adjust their positions significantly throughout the exchange process, serving primarily as an “external” potential to stabilize the crystal in the active layer. In the strong interlayer coupling limit ($d/a \ll 1$), the electrons in the passive layer participate more in the exchange, making larger excursions from their equilibrium positions.

This evolution is quantified in Fig. 15, where we present the maximal displacement r_{max} of an electron in the passive layer from its equilibrium position as a func-

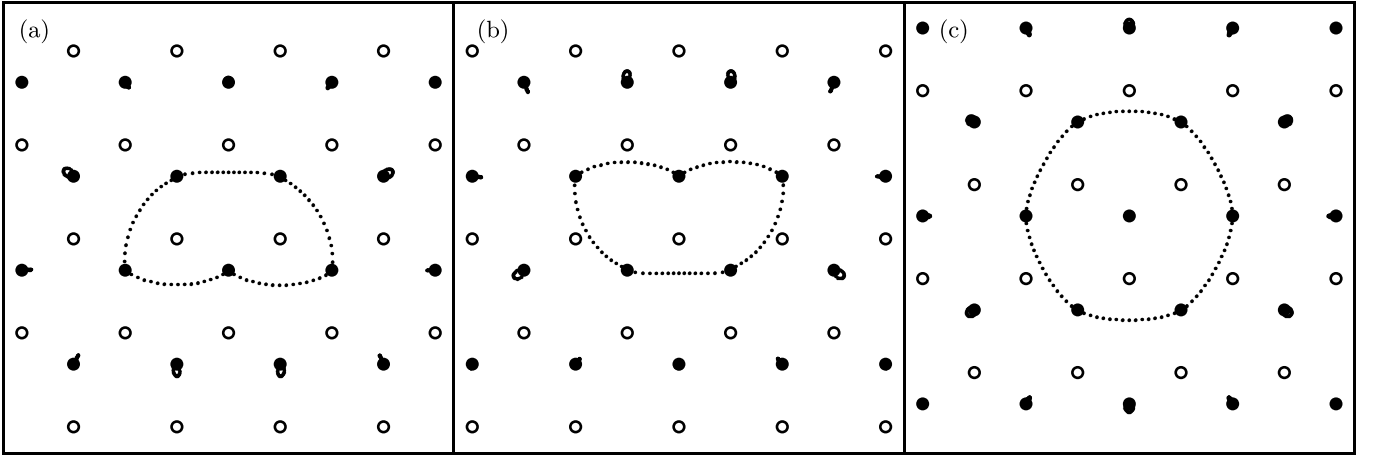


FIG. 16. Paths for (a,b) 5, and (c) 6-particle exchange in the staggered triangular geometry (Phase V) for interlayer separation $d/a \approx 1.5$. We refer to the inequivalent 5-particle exchange paths in Panels (a) and (b) as 5 and 5^* , respectively.

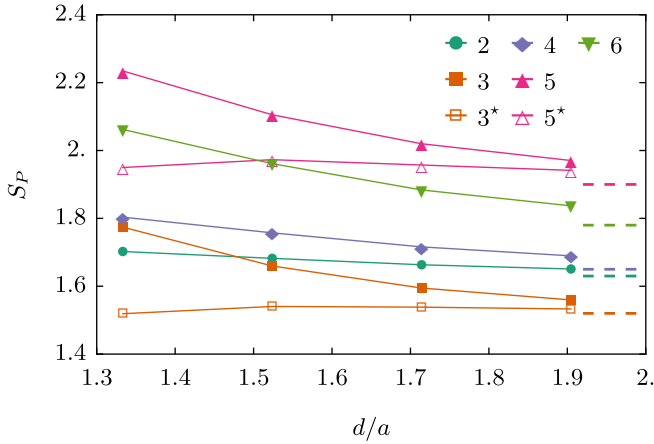


FIG. 17. Actions for 2,3,4,5, and 6 particle exchange in Phase V. The distinction between paths 3/3* and 5/5* is in the nearest neighbors from the opposite layer (see Fig. 2 and Fig. 16, respectively). Dashed lines are the values of the corresponding actions in the monolayer limit $d \rightarrow \infty$.

tion of d/a . For $d/a \gtrsim 1$, we indeed find that r_{\max} does not exceed roughly 10% of the BLWC lattice constant a_ℓ for all the exchange process considered. On the other hand, when $d/a \rightarrow 0$ the displacements can be on the order of the lattice constant, depending on the particular exchange process. This evolution of the passive layer displacements can also be qualitatively inferred from the paths shown in Figs. 2-5.

Appendix C: Larger exchange cycles

In general, the interlayer coupling tends to reduce the importance of large exchange cycles in the BLWC relative to the monolayer. To the extent we expect such cycles to play a role in determining the magnetic ground state, this will most likely be for larger values of d/a . In Fig. 16 we therefore also report the exchange paths associated with 5 and 6-particles exchange in Phase V for $d/a \approx 1.5$, with the corresponding actions shown in Fig. 17 as a function d/a . Except paths 3* and 5* (shown in Figs. 2c and 16b, respectively), the actions are monotonically increasing with decreasing d/a .

-
- [1] E. Wigner, On the interaction of electrons in metals, *Phys. Rev.* **46**, 1002 (1934).
 - [2] L. Bonsall and A. A. Maradudin, Some static and dynamical properties of a two-dimensional wigner crystal, *Phys. Rev. B* **15**, 1959 (1977).
 - [3] Y. M. Vil'k and Y. P. Monarkha, *Fiz. Nizk. Temp.* **10**, 886 (1984); **11**, 971 (1985).
 - [4] V. I. Falko, Optical branch of magnetophonons in a double-layer wigner crystal, *Phys. Rev. B* **49**, 7774 (1994).
 - [5] S. Narasimhan and T.-L. Ho, Wigner-crystal phases in bilayer quantum hall systems, *Phys. Rev. B* **52**, 12291 (1995).
 - [6] K. Esfarjani and Y. Kawazoe, A bilayer of wigner crystal in the harmonic approximation, *Journal of Physics: Condensed Matter* **7**, 7217 (1995).
 - [7] G. Goldoni and F. M. Peeters, Stability, dynamical properties, and melting of a classical bilayer wigner crystal, *Phys. Rev. B* **53**, 4591 (1996).
 - [8] G. Goldoni and F. M. Peeters, Wigner crystallization in quantum electron bilayers, *Europhysics Letters* **37**, 293 (1997).
 - [9] In Ref. [7] it was concluded that there is a non-zero range near $d/a = 0$ where a single-component triangular lattice

- is stable (Phase I). It was later shown, however, that the single-component triangular lattice is stable only at $d/a = 0$ [41], with the aspect ratio in Phase II evolving continuously down to $d/a = 0$.
- [10] L. Świerkowski, D. Neilson, and J. Szymański, Enhancement of wigner crystallization in multiple-quantum-well structures, *Phys. Rev. Lett.* **67**, 240 (1991).
- [11] F. Rapisarda and G. Senatore, Diffusion monte carlo study of electrons in two-dimensional layers, *Australian journal of physics* **49**, 161 (1996); Recent progress on the phase diagram of coupled electron layers in zero magnetic field, in *Strongly Coupled Coulomb Systems*, edited by G. J. Kalman, J. M. Rommel, and K. Blagoev (Springer US, Boston, MA, 1998) pp. 529–532.
- [12] B. Tanatar and D. M. Ceperley, Ground state of the two-dimensional electron gas, *Phys. Rev. B* **39**, 5005 (1989).
- [13] C. Attaccalite, S. Moroni, P. Gori-Giorgi, and G. B. Bachelet, Correlation energy and spin polarization in the 2d electron gas, *Phys. Rev. Lett.* **88**, 256601 (2002).
- [14] N. D. Drummond and R. J. Needs, Phase diagram of the low-density two-dimensional homogeneous electron gas, *Phys. Rev. Lett.* **102**, 126402 (2009).
- [15] S. Azadi, N. D. Drummond, and S. M. Vinko, Quantum monte carlo study of the phase diagram of the two-dimensional uniform electron liquid (2024), arXiv:2405.00425 [cond-mat.str-el].
- [16] Y. Zhou, J. Sung, E. Brutschea, I. Esterlis, Y. Wang, G. Scuri, R. J. Gelly, H. Heo, T. Taniguchi, K. Watanabe, G. Zaránd, M. D. Lukin, P. Kim, E. Demler, and H. Park, Bilayer Wigner crystals in a transition metal dichalcogenide heterostructure, *Nature* **595**, 48 (2021).
- [17] T. Smoleński, P. E. Dolgirev, C. Kuhlenkamp, A. Popert, Y. Shimazaki, P. Back, X. Lu, M. Kroner, K. Watanabe, T. Taniguchi, I. Esterlis, E. Demler, and A. Imamoğlu, Signatures of Wigner crystal of electrons in a monolayer semiconductor, *Nature* **595**, 53 (2021).
- [18] D. J. Thouless, Exchange in solid ^3He and the heisenberg hamiltonian, *Proceedings of the Physical Society* **86**, 893 (1965).
- [19] M. Roger, J. H. Hetherington, and J. M. Delrieu, Magnetism in solid ^3He , *Rev. Mod. Phys.* **55**, 1 (1983).
- [20] M. Roger, Multiple exchange in ^3He and in the wigner solid, *Phys. Rev. B* **30**, 6432 (1984).
- [21] M. Katano and D. S. Hirashima, Multiple-spin exchange in a two-dimensional wigner crystal, *Phys. Rev. B* **62**, 2573 (2000).
- [22] C. N. Sudip Chakravarty, Steven Kivelson and K. Voelker, Wigner glass, spin liquids and the metal-insulator transition, *Philosophical Magazine B* **79**, 859 (1999), <https://doi.org/10.1080/13642819908214845>.
- [23] K. Voelker and S. Chakravarty, Multiparticle ring exchange in the wigner glass and its possible relevance to strongly interacting two-dimensional electron systems in the presence of disorder, *Phys. Rev. B* **64**, 235125 (2001).
- [24] S. Coleman, The uses of instantons, in *The Whys of Subnuclear Physics*, edited by A. Zichichi (Springer US, Boston, MA, 1979) pp. 805–941.
- [25] D. S. Hirashima, Magnetism of a bilayer wigner crystal, *Journal of the Physical Society of Japan* **70**, 931 (2001).
- [26] B. Bernu, L. Cândido, and D. M. Ceperley, Exchange frequencies in the 2d wigner crystal, *Phys. Rev. Lett.* **86**, 870 (2001).
- [27] Throughout the text we quote approximate, as opposed to exact, values of d/a , writing $d/a \approx \dots$. The reason is that, in the numerical calculations, we actually fix the ratio d/a_ℓ , where a_ℓ is the lattice constant for a given BLWC geometry. The interparticle distance a is related to a_ℓ according to $a = \sqrt{A_c/\pi}$, where A_c is the unit cell area. In the different geometries we have $A_c = \sqrt{3}a_\ell^2/2$ (Phase V), $A_c = \sin\theta a_\ell^2$ (Phase IV), $A_c = a_\ell^2$ (Phase III), and $A_c = ra_\ell^2$ (Phase II).
- [28] A. Läuchli, J. C. Domenge, C. Lhuillier, P. Sindzingre, and M. Troyer, Two-step restoration of $\text{su}(2)$ symmetry in a frustrated ring-exchange magnet, *Phys. Rev. Lett.* **95**, 137206 (2005).
- [29] There are two symmetry-related 4-particle exchange paths in Phase II (Fig. 5d) and the exchange coupling J_4 is therefore multiplied by a factor of two.
- [30] When $d/a = 0$ the paths become identical to the same paths for a single-layer WC, although the meaning of 3 and 4 particle exchange is different from the single-layer case.
- [31] K.-S. Kim, I. Esterlis, C. Murthy, and S. A. Kivelson, Dynamical defects in a two-dimensional wigner crystal: Self-doping and kinetic magnetism, *Phys. Rev. B* **109**, 235130 (2024).
- [32] G. Misguich, B. Bernu, C. Lhuillier, and C. Waldtmann, Spin liquid in the multiple-spin exchange model on the triangular lattice: ^3He on graphite, *Phys. Rev. Lett.* **81**, 1098 (1998); G. Misguich, C. Lhuillier, B. Bernu, and C. Waldtmann, Spin-liquid phase of the multiple-spin exchange hamiltonian on the triangular lattice, *Phys. Rev. B* **60**, 1064 (1999).
- [33] T. Momoi, P. Sindzingre, and K. Kubo, Spin nematic order in multiple-spin exchange models on the triangular lattice, *Phys. Rev. Lett.* **108**, 057206 (2012).
- [34] P. Chandra, P. Coleman, and A. I. Larkin, Ising transition in frustrated heisenberg models, *Phys. Rev. Lett.* **64**, 88 (1990).
- [35] O. A. Starykh, Unusual ordered phases of highly frustrated magnets: a review, *Reports on Progress in Physics* **78**, 052502 (2015), and references therein
- [36] The putative transition between the VBS and Néel state in Phase III is of particular interest, as such a transition has been argued to proceed via a deconfined quantum critical point. While interesting field-theories for the staggered VBS to Néel transition have been proposed [42], numerical work [43] suggests the transition in the staggered VBS case is likely to be first-order.
- [37] J. Sung, J. Wang, I. Esterlis, P. A. Volkov, G. Scuri, Y. Zhou, E. Brutschea, T. Taniguchi, K. Watanabe, Y. Yang, M. A. Morales, S. Zhang, A. J. Millis, M. D. Lukin, P. Kim, E. Demler, and H. Park, Observation of an electronic microemulsion phase emerging from a quantum crystal-to-liquid transition (2023), arXiv:2311.18069 [cond-mat.str-el].
- [38] K.-S. Kim, C. Murthy, A. Pandey, and S. A. Kivelson, Interstitial-induced ferromagnetism in a two-dimensional wigner crystal, *Phys. Rev. Lett.* **129**, 227202 (2022).
- [39] The importance of kinetic magnetism in triangular lattice Hubbard models has also been recently emphasized [44].
- [40] Castaing, B., A model for exchange in liquid ^3He , *J. Physique Lett.* **41**, 333 (1980).
- [41] L. Šamaj and E. Trizac, Critical phenomena and phase sequence in a classical bilayer wigner crystal at zero tem-

- perature, Phys. Rev. B **85**, 205131 (2012).
- [42] C. Xu and L. Balents, Quantum phase transitions around the staggered valence-bond solid, Phys. Rev. B **84**, 014402 (2011).
- [43] A. Sen and A. W. Sandvik, Example of a first-order n el to valence-bond-solid transition in two dimensions, Phys. Rev. B **82**, 174428 (2010).
- [44] L. Ciorciaro, T. Smoleński, I. Morera, N. Kiper, S. Hies-tand, M. Kroner, Y. Zhang, K. Watanabe, T. Taniguchi, E. Demler, *et al.*, Kinetic magnetism in triangular moir  materials, Nature **623**, 509 (2023); I. Morera and E. Demler, Itinerant magnetism and magnetic polarons in the triangular lattice Hubbard model, arXiv preprint arXiv:2402.14074 (2024).